Subharmonic resonance of oblique interfacial waves by a progressive surface wave

By D. F. Hill and M. A. Foda

Environmental Water Resources, Department of Civil Engineering,
University of California at Berkeley, Berkeley, CA 94720, USA

Experimental and theoretical investigations into the generation of internal gravity waves by monochromatic progressive surface waves are presented. Using the method of nonlinear resonant interactions, a triad consisting of a single surface wave and two oblique internal waves in a two-layer model is considered. A multiple scales analysis is adopted and the boundary value problem is expanded in a power series of the surface-wave steepness. At the leading order, the linear harmonics are obtained and the conditions for resonance are determined. A second-order analysis is then used to derive temporal evolution equations for the internal-wave amplitudes. As a consequence of having a single generating train of the surface waves, two oblique trains of internal waves of much shorter wavelength are found to be resonated exponentially in time. Both linear and nonlinear bounds on surface-wave frequency, density ratio and interaction angle are found, demonstrating that the instability is highly narrow banded. It is found that the internal waves grow most rapidly at the linear cut-off values. Experimental evidence is presented and demonstrates good agreement with the theoretical results. Discussion of an application of the theory to the nonlinear energy transfer between very-low-frequency waves in the deep ocean is then provided.

Keywords: subharmonic resonance; internal waves; parametric instability

1. Introduction

The generation of internal waves in a stratified system is a problem of obvious practical interest and one which has received a great deal of attention. Of particular interest among the numerous possible generating mechanisms is that of generation by surface waves. Ting & Raichlen (1986) used a purely linear analysis to quantify the linear resonance of internal waves inside a trench of finite width.

Ball (1964) used a second-order nonlinear resonance theory to demonstrate that linear growth of an internal wave could result from the interactions between two finite-amplitude surface waves. Similar studies were undertaken by Thorpe (1966), Hasselmann (1966) and Brekhovskikh *et al.* (1972). Fundamental to all of these analyses was that two surface waves were required to resonate a single internal wave.

Watson *et al.* (1976) extended this concept by considering how a spectrum of surface waves could generate a corresponding spectrum of internal waves. Their work considered specifically the limit in which the internal waves had much lower frequencies and longer wavelengths than that of the surface waves. It was hypothesized that energy could then be cascaded down to shorter internal waves via interactions between internal waves.

D. F. Hill and M. A. Foda

Experimental studies of this triad were undertaken by Joyce (1974) and Lewis *et al.* (1974). The former author specifically investigated a triad consisting of two standing surface waves and a single standing internal wave. In this case, the interactions between the two surface waves resonated the internal wave. The latter authors considered instead the perturbation to a surface wave induced by the presence of an internal wave. Thus, the interactions between the surface and internal waves resonated a second surface wave.

Common to all of these studies, both theoretical and experimental, is that the wave triad consisted of two surface waves and a single internal wave. Motivated by the desire to instead describe internal-wave evolution by a single surface wave, Hill & Foda (1996) considered, for the first time, a triad consisting of two perturbation internal waves and a single finite-amplitude surface wave. The implications of this are considerable for two reasons. First, natural sea states are commonly described by narrow-banded spectra (see, for example, Pierson & Moskowitz 1964) where energy is clustered around a mean frequency and direction. Therefore, the adoption of a monochromatic surface-wave field may be viewed as a realistic representation of such narrow-banded sea states. Second, a single wave is now the primary carrier of energy, and resonates the other two waves via exponential, rather than linear, growth. This is clearly a much stronger interaction and assures that, no matter how small the initial disturbances, the internal waves will grow to finite amplitudes. Instead of two pre-existing surface waves of finite amplitude and specific orientation resonating a single internal wave linearly in time, a single train of surface waves is now all that is required to resonate two internal-wave trains exponentially in time. Furthermore, unlike earlier studies, the proposed mechanism provides for a direct energy transfer into the short range of internal-wave wavelengths.

The authors considered the limit in which all three waves were plane and parallel, with the internal waves travelling in opposite directions. Furthermore, as motivated by laboratory observations, the surface wave was assumed to be much longer than the internal waves. In the limit of two inviscid layers, no growth was found. Weak viscosity was then introduced into the lower layer and, through use of a boundary layer approximation, it was shown that the internal waves did grow exponentially in time.

The current paper extends the previous work by relaxing the restriction that the three waves be plane and parallel. Additionally, no approximations are made based on the relative magnitudes of the wavenumber vectors. Linear analysis and the imposition of appropriate resonance conditions yield the internal-wave parameters as functions of the physical properties of the system and the surface-wave frequency. It is found that there is a surface-wave cut-off frequency below which a resonant triad cannot exist. This is seen to correspond to the case of exact subharmonic parametric instability, where the internal waves propagate at equal and opposite angles to the surface wave.

Utilizing a perturbation expansion of the velocity potential in surface-wave steepness and carrying the analysis to the second order, it is found that substantial growth exists in the inviscid limit. This, contrasted with the previous results of Hill & Foda (1996), highlights the significance of the internal waves being allowed to be oblique to the generating surface wave. It is found that the most unstable internal wave modes occur at the surface-wave cut-off frequency. Furthermore, the nonlinear analysis reveals that there is an upper bound on surface-wave frequency, beyond which, even though a resonant triad exists, no growth is found.
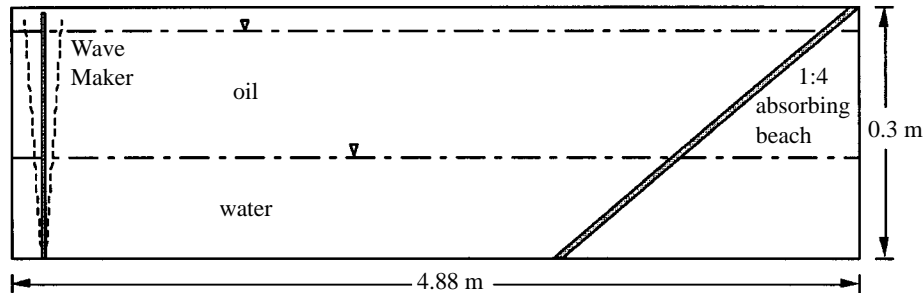
Figure 1. Experimental set-up.

Measurements of internal-wave growth in a small flume are presented and compared with the theoretical results. The measured internal wave frequencies are in excellent agreement with those predicted by the linear analysis. Furthemore, the measured band of frequency within which growth occurs agrees very well with the theory. The experimentally determined internal-wave growth rates are found to be of the same order as the theoretical predictions.

Applications of the theory to estuarine and open-ocean scales are then considered. In particular, the nonlinear energy transfer from barotropic tides to near-inertial baroclinic modes is suggested as a possible manifestation of this mechanism.

2. Experimental investigation

(a) Set-up

The earlier experiments reported by Hill & Foda (1996) involved a two-layer system of water over fluidized sediment. The practical difficulties of obtaining detailed quantitative data with this set-up led the authors to construct a new experimental apparatus. The goal was to study the dynamics of the interface between two immiscible fluids on a small scale. A flume was constructed of 95 mm thick Plexiglas, having a length $L = 4.88$ m, a depth $D = 30$ cm, and a width $W = 15$ cm. A hinged wavemaker, driven by a rotary motor, was placed at one end of the tank. Note that the paddle of the wavemaker extended to the bottom of the flume, and that only the barotropic mode was generated by its motion. The waves were absorbed at the other end of the tank by a $1:4$ sloping beach constructed of a fibrous horsehair type material. The details of the experimental set-up are shown in figure 1.

Originally, it was desired to have water as the upper fluid and a non-conducting fluid as the lower. In this manner, resistance wave gauges could be used to make simultaneous measurements of the free surface and the interface (see Lewis *et al.* 1974). However, this configuration was decided against, due to the safety and environmental concerns associated with handling fluids such as carbon tetrachloride or freon. As a result, light mineral oil was used for the upper layer and fresh water for the lower, yielding a density ratio of $\gamma \equiv (\rho/\rho') = 0.85$, where ρ is the density of the mineral oil and ρ' is the density of the water. A consequence of this, of course, was that data via resistance wave gauges could be obtained at the interface only.

To address the significance of both free surface and interfacial tension in the laboratory experiments, note that a typical value of surface tension for water is 0.07 N m^{-1}. Consequently (see Lamb 1932, art. 267), the capillary length scale is approximately 1.7 cm. This is fully two orders of magnitude shorter than the wavelengths of the free

surface waves mechanically generated in the laboratory experiments. At the interface, note that a typical value of interfacial tension between mineral oil and water is $0.05 \, \text{N} \, \text{m}^{-1}$. This value, combined with the known density ratio of 0.85, leads to an interfacial capillary length scale of approximately 3.7 cm. The internal waves resonated in the experiments had wavelengths one order of magnitude greater than this. Given that both the free surface and internal wavelengths are much greater than the free surface and interfacial capillary wavelengths, omission of surface and interfacial tension in the subsequent theoretical analysis is justified.

The data acquisition system consisted of two gauges located at 1 m and 3.2 m downstream of the wavemaker. Both were postitioned at a distance of 2.5 cm from the side wall of the tank. The gauges penetrated both fluid layers so as to provide accurate measurement of the interfacial displacement. A multi-probe isolator and amplifier (Daytronic Model 9005) connected the gauges to a PC equipped with a UPC card.

(*b*) *Procedure and analysis*

The gauges were calibrated in 5 mm increments at the beginning of each set of experimental runs, with the data being fitted to a linear curve. While remarkably consistent, the gauges were nonetheless recalibrated frequently to account for changes in ambient temperature. Four parameters could be varied with the set-up as described: the two fluid layer depths, surface-wave frequency and surface-wave amplitude. Runs were conducted for three different combinations of layer depths: $H = 10.5$ cm and $h = 10.5$ cm; $H = 12.5$ cm and $h = 7.9$ cm; and $H = 13.6$ cm and $h = 5.5$ cm, where H is the upper layer depth and h the lower layer depth. In turn, for each depth configuration, numerous runs were conducted at various frequencies and amplitudes.

Before beginning detailed experimental runs, it was desirable to determine the effectiveness of the beach at absorbing the waves generated by the wavemaker. This would allow for an estimate of what percentage of the incident wave field was being reflected back into the tank. To facilitate this, a single pulse of the wavemaker was generated, sending a packet of waves down the tank. As this packet impinged upon the beach, a certain portion of the wave energy was dissipated and the rest was reflected back into the tank as a packet with severely reduced amplitude. As a crude measure of the reflectivity of the beach, the maximum amplitude of the reflected packet was compared to the maximum amplitude of the incident packet. It was found that the ratio of these amplitudes was of the order of 5%.

In each experimental run, data were collected at 50 Hz for a period of 300 s. Depending upon the frequency and amplitude of the surface wave, significant subharmonic motion at the interface would or would not be visually detected. Figure 2 shows a series of three photographs during a typical experimental run where subharmonic internal waves were detected. Note that the lower fluid has been dyed to make the interface more visible. The total fluid depth is 21 cm and the waves are propagating from right to left.

In the first photograph, a large amplitude internal wave is seen. Note that the interface is tilted towards the camera, so that the crest of the internal wave is on the back wall of the flume and the trough of the internal wave is on the front wall. It is clear that, in the cross-tank direction, the lowest mode has been excited. Furthermore, it is clear from this image that the internal-wave vectors are highly oblique to the surface-wave vector, which points down the tank. In the second image, which is at one surface-wave period later in time, the interface is 180° out of phase so that
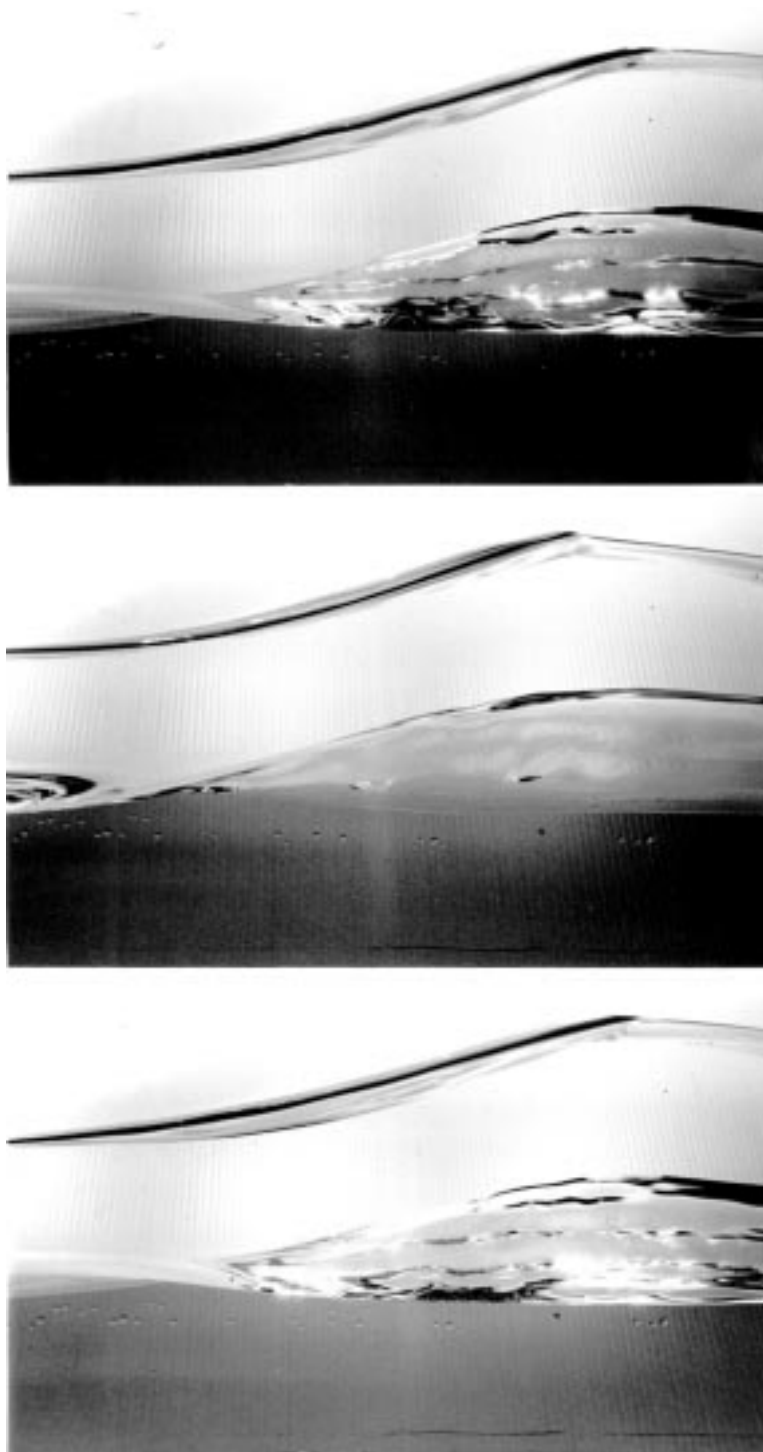
Figure 2. Photographs of typical experimental run. The images are spaced at intervals of one surface-wave period and demonstrate that the internal waves are subharmonic and highly oblique to the surface wave. Note that the total fluid depth is 21 cm and that the direction of wave propagation is from right to left.
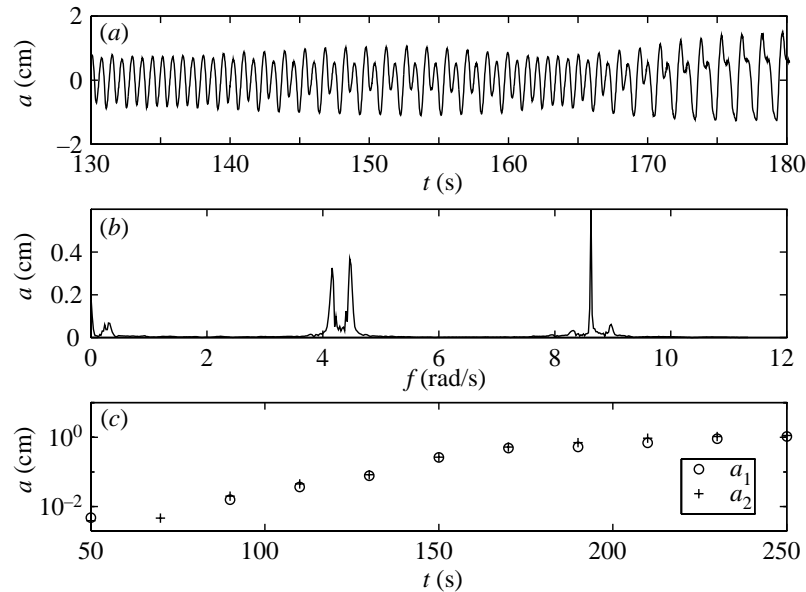
Figure 3. (*a*) Sample interfacial time series demonstrating development of subharmonic internal waves. (*b*) Amplitude spectrum indicating the three peaks associated with the three waves of the resonant triad. Note that the sum of the two low-frequency internal waves is equal to the frequency of the surface wave. (*c*) Harmonic analysis of time series showing the evolution of the internal-wave amplitudes. $H = 12.5$ cm, $h = 7.9$ cm, $\lambda_z = 20.6$ m^{-1}, $\gamma = 0.85$.

the crest of the internal wave is now on the front wall of the tank. In the final image, which was taken at two suface wave periods after the first image, the interface looks largely as it did in the first image. Therefore, it is clear that the interfacial waves are subharmonic to the surface wave. It was visually observed that the internal-wave pattern slowly propagated down the flume, indicating that the internal-wave vectors were not exactly normal to the surface-wave vector.

A segment of a sample internal-wave time series is show in the first portion of figure 3. The segment shown is roughly the third minute of the experimental run and demonstrates the first indication of subharmonic wave generation. At the start of the time series, the interface is oscillating in phase with the surface wave, but as time progresses, a clear period doubling is apparent. This indicates the presence of subharmonic internal waves. The beating seen is due to the fact that the frequencies of the resonated internal waves are not exactly equal. By taking the Fourier transform of the wave record, the three frequencies, one due to the surface wave and two due to the internal waves, could be ascertained. The second portion of figure 3 illustrates this. The peak with the highest frequency is that of the surface wave. The two peaks which are close together and at lower frequency are those of the internal waves. Note that the internal-wave frequencies are nearly equal and are subharmonic to the surface wave. Finally, with the frequencies determined, a harmonic analysis could be performed in order to determine the evolution of the internal-wave amplitudes. This is shown in the last portion of figure 3. The internal-wave amplitudes clearly grow with time. Note that the data here are plotted on a semilog axis, so that this final plot, which can be fit to a straight line, represents exponential growth. With this for motivation, attention is turned to the theoretical formulation of the problem and a comparison of the theoretical and experimental results.
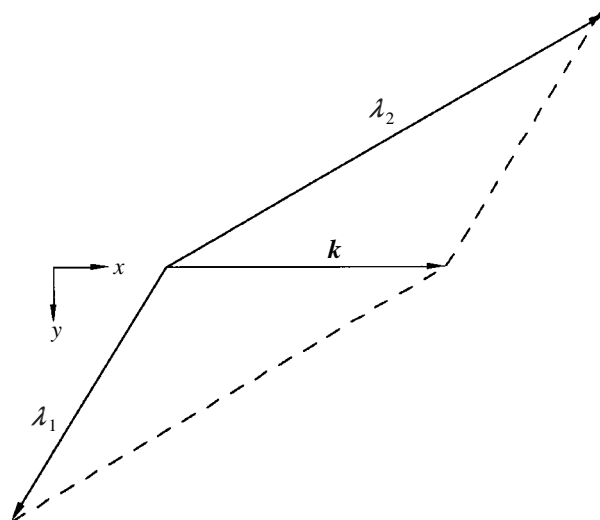
Figure 4. Triad wave vector orientation.

3. Theoretical formulation

The origin of a three-dimensional Cartesian coordinate system is placed on the undisturbed interface between an inviscid surface layer of depth H and density ρ, and an inviscid lower layer of depth h, density ρ'. The y-coordinate is defined as pointing vertically upward and the x- and z-coordinates define the horizontal. The density ratio $\gamma = (\rho/\rho')$ is assumed to be less than unity. To the leading order, the wave field is made up of a linear progressive surface wave of amplitude A, wave vector $\bar{k}$ and frequency ω. The vector, $\bar{k}$, is aligned with the positive x-axis. The displacement η of the free surface from its equilibrium value of $y = H$ is therefore given by

$$\eta = A\mathrm{e}^{\mathrm{i}(kx-\omega t)}.$$

The interface will oscillate synchronously with η, with a reduced amplitude A_r in response to the passage of the surface wave. In addition, perturbation internal waves of amplitudes a_1 and a_2, wave vectors $\bar{\lambda}_1$ and $\bar{\lambda}_2$ and frequencies σ_1 and σ_2 are introduced. Therefore, the displacement, ξ, of the interface from its equilibrium value of $y = 0$ is given by

$$\xi = A_\mathrm{r}\mathrm{e}^{\mathrm{i}(kx-\omega t)} + a_1\mathrm{e}^{\mathrm{i}(\lambda_{1x}x+\lambda_{1z}z-\sigma_1 t)} + a_2\mathrm{e}^{\mathrm{i}(\lambda_{2x}x+\lambda_{2z}z-\sigma_2 t)} + \xi_\mathrm{nl},$$

where ξ_nl refers to the bound nonlinear displacement due to interactions between the three linear wave harmonics. The orientations of the wavenumber vectors are detailed in figure 4. Note that a_1, a_2 and A are taken to be complex and σ_1 and σ_2 are defined to be positive real values. Furthermore, a_1 and a_2 are taken to be functions of a slow time scale, t_1. In a similar manner, slow spatial variation of the resonated internal waves may be included. This is omitted in the current analysis, however, as the *time* scale of the interaction is of paramount interest. For second-order interactions to occur, the phase functions of the two internal waves must sum up to equal the phase function of the surface wave. This requires satisfaction of the following conditions:

$$\bar{\lambda}_2 + \bar{\lambda}_1 = \bar{k}, \tag{3.1}$$

$$\sigma_1 + \sigma_2 = \omega. \tag{3.2}$$

The first of these conditions merely dictates that the wave vectors of the three waves form a triangle in the x–z plane. The second requires that the internal wave frequencies sum up to equal the surface-wave frequency.

Turning to the governing equations and boundary conditions, the assumption of potential flow and use of incompressible continuity reveal that the velocity potential is governed by Laplace's equation throughout the depth of the fluid:

$$\nabla^2 \Phi = 0, \quad -h \leqslant y \leqslant H + \eta. \tag{3.3}$$

At the free surface, the usual dynamic and kinematic conditions are given by

$$\Phi_t + g\eta + \tfrac{1}{2}\nabla \Phi \cdot \nabla \Phi = 0, \quad y = H + \eta, \tag{3.4}$$

$$\mathrm{D}\eta/\mathrm{D}t = \Phi_y, \quad y = H + \eta. \tag{3.5}$$

Note the absence of surface tension in (3.4), as was justified in the previous section.

At the interface, there are similar conditions of continuity of normal stress and velocity.

$$\rho(\Phi_t + g\xi + \tfrac{1}{2}\nabla \Phi \cdot \nabla \Phi)^+ = \rho'(\Phi_t + g\xi + \tfrac{1}{2}\nabla \Phi \cdot \nabla \Phi)^-, \quad y = \xi, \tag{3.6}$$

$$\mathrm{D}\xi/\mathrm{D}t = \Phi_y^+ = \Phi_y^-, \quad y = \xi. \tag{3.7}$$

Again, interfacial tension has been omitted due to the disparity between the wavelengths of the resonated internal waves and the characteristic length scale of interfacial capillary waves. Note that the $+$ and $-$ superscripts denote evaluation just above and just below the interface, respectively. Finally, the no-flow bottom boundary condition is simply

$$\Phi_y = 0, \quad y = -h. \tag{3.8}$$

4. Solution

The velocity potential, Φ, is expanded in a power series of a small parameter ϵ:

$$\Phi = \epsilon\phi\mathrm{e}^{\mathrm{i}(kx-\omega t)} + \epsilon^2\{\psi\mathrm{e}^{\mathrm{i}(\lambda_{1x}x+\lambda_{1z}z-\sigma_1 t)} + \chi\mathrm{e}^{\mathrm{i}(\lambda_{2x}x+\lambda_{2z}z-\sigma_2 t)} + q(\phi,\phi)\} \tag{4.1}$$

$$+\epsilon^3\{\cdots + \psi'\mathrm{e}^{\mathrm{i}(\lambda_{1x}x+\lambda_{1z}-\sigma_1 t)} + \chi'\mathrm{e}^{\mathrm{i}(\lambda_{2x}x+\lambda_{2z}z-\sigma_2 t)} + \cdots\} + \mathrm{c.c.}, \tag{4.2}$$

where the expansion parameter is taken to be given by the steepness of the surface wave:

$$\epsilon = kA.$$

In the expansion for Φ, the first three terms are the linear harmonics describing the interacting wave triad. The analysis is restricted to the case of small internal waves only so the internal wave harmonics appear at $O(\epsilon^2)$ and not at $O(\epsilon)$. Recall that a_1 and a_2 are functions of the slow time scale, which, with the introduction of the expansion parameter can be formalized as $t_1 = \epsilon t$. The fourth term represents the forced motion due to self interaction of the surface wave. Terms in the second bracket are forced harmonics due to interactions between the surface wave and the internal waves, and c.c. denotes the complex conjugate. To clarify what is meant by a forced harmonic, note for example that the product of $\phi\exp\{\mathrm{i}(kx - \omega t)\}$ and $\psi\exp\{\mathrm{i}(\lambda_{1x}x + \lambda_{1z}z - \sigma_1 t)\}$ yields, with the help of the resonance conditions (3.1), (3.2), a term that is in phase with $\chi\exp\{\mathrm{i}(\lambda_{2x}x + \lambda_{2z}z - \sigma_2 t)\}$. Such terms will then provide boundary forcing in the inhomogeneous boundary value problem for χ'.
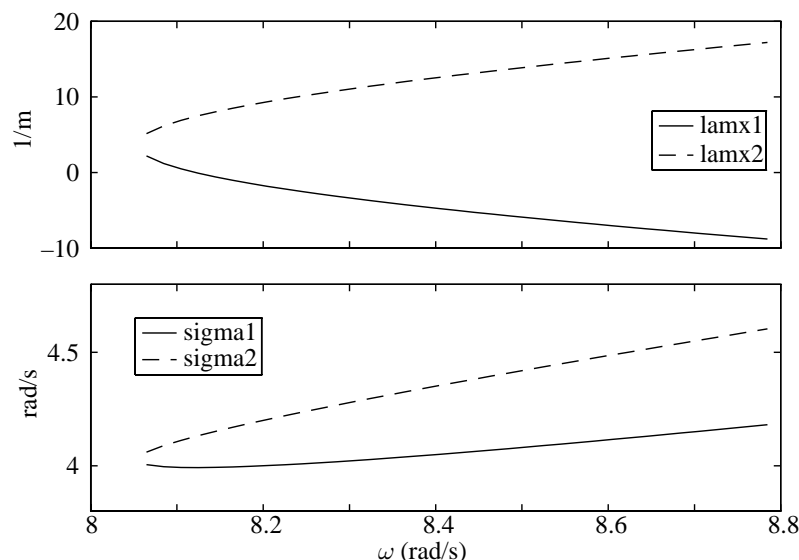
Figure 5. Internal wave frequencies and x-direction internal wave-vector components as functions of ω. $H = 10.5$ cm, $h = 10.5$ cm, $\gamma = 0.85$, $\lambda_z = 20.6$ m^{-1}.

(*a*) *Linear solutions*

The linear harmonics all satisfy Laplace's equation (3.3) and the linear versions of the boundary conditions (3.4)–(3.8). Solution for the velocity potentials and dispersion relationships of the three harmonics is quite straightforward (see Lamb 1932, art. 231) and is not presented here.

So if the fluid layer depths and densities are known and the surface-wave frequency is specified, five equations exist for six unknowns. The equations are (3.1), (3.2) and the two internal-wave dispersion relationships. The unknowns are σ_1, σ_2, λ_{1x}, λ_{2x}, λ_{1z} and λ_{2z}. It is clear that by allowing for the internal waves to be oblique, two new unknowns, but only one new equation have been introduced. Therefore, the components of the internal-wave vectors in the z-direction, which must be equal and opposite, are free parameters. Once a value is chosen for $\lambda_z \equiv \lambda_{1z} = -\lambda_{2z}$, the remaining internal-wave parameters may be determined.

As an example, it was visually observed in the laboratory that the width of the flume contained one half of an internal-wave wavelength. Thus, $\lambda_z \equiv (\pi/W)$. Figure 5 details the internal-wave parameters as functions of ω for the case where $H = 10.5$ cm and $h = 10.5$ cm. Note that there is a surface-wave frequency, a cut-off frequency, below which resonant triads do no exist. This cut-off frequency is a function of H, h, γ and λ_z. Furthermore, the critical frequency corresponds to the case in which the internal waves are exactly subharmonic to the surface wave, i.e. $\sigma_1 = \sigma_2 = \frac{1}{2}\omega$, and are propagating at equal and opposite angles to the surface wave. Therefore, the linear theory is able to identify the conditions under which resonant triads exist. As will be shown subsequently, this existence of a triad is certainly necessary for the resonance of internal waves, but is not sufficient.

(*b*) *Forced harmonics*

With the linear harmonics determined, solution of the second-order inhomogeneous boundary-value problem can be pursued. Note that at this order, boundary forcing

arises from quadratic interactions between the linear harmonics. As a result of the homogeneous, first order problem having a non-trivial solution, the inhomogeneous second-order problem has a solution only if the forcing terms are orthogonal to the homogeneous solution. This introduces a solvability condition, known as the Fredholm alternative, which is obtained by applying Green's theorem.

For example, to solve for χ', which represents the forced second-order harmonic in phase with χ, (4.2) is substituted into the governing equation and boundary conditions. Then, terms proportional to ϵ^3 and $\exp\{i(\lambda_{2x}x + \lambda_{2z}z - \sigma_2 t)\}$ are collected to yield the inhomogeneous problem. Applying Green's theorem to χ' and χ across the depths of both layers yields

$$\int_0^H (\chi\chi'_{yy} - \chi'\chi_{yy})\,\mathrm{d}y = [\chi\chi'_y - \chi'\chi_y]_0^H,$$

$$\int_{-h}^0 (\chi\chi'_{yy} - \chi'\chi_{yy})\,\mathrm{d}y = [\chi\chi'_y - \chi'\chi_y]_{-h}^0.$$

With manipulation, these equations lead to the following evolution equation:

$$\frac{\mathrm{d}a_2}{\mathrm{d}t} = i\alpha_2 a_1^* A. \tag{4.3}$$

The interaction coefficient α_2 is a purely real coefficient whose length precludes its display here.

Repeating this process for the other internal forced harmonic, ψ', yields the second evolution equation.

$$\frac{\mathrm{d}a_1}{\mathrm{d}t} = i\alpha_1 a_2^* A. \tag{4.4}$$

Presentation and discussion of the interaction coefficients is provided in the Appendix. Cross differentiation of (4.3) and (4.4) reveals that the internal wave amplitudes are governed by exponentials.

$$a_1, a_2 \propto \mathrm{e}^{\pm\sqrt{-\alpha_1\alpha_2}At}. \tag{4.5}$$

Clearly, if the interaction coefficients are of the same sign, there is no growth and the only result is a modulation of the frequencies of the internal waves. If the interaction coefficients are of opposite signs however, the square root is a real value and the amplitudes of the internal waves grow exponentially in time.

5. Theoretical results and comparison

To validate the theoretical formulation, comparisons between theory and experiment were made for each of the three experimental depth configurations. Considering first the linear theory, the internal-wave frequencies obtained from spectral analysis were compared to the predicted values. This is detailed in figures 6a–c. The error bars indicate the uncertainty in both the surface-wave frequency and the internal-wave frequencies, due to the resolution of the FFT of the interfacial time series. Clearly, there is excellent agreement, indicating that the triad postulated was indeed the one observed in the laboratory. Of interest is that the differences observed between theory and experiment are very systematic. This is most likely due to the influence of viscosity, in the form of oscillatory boundary layers on the side walls and bottom of the flume.
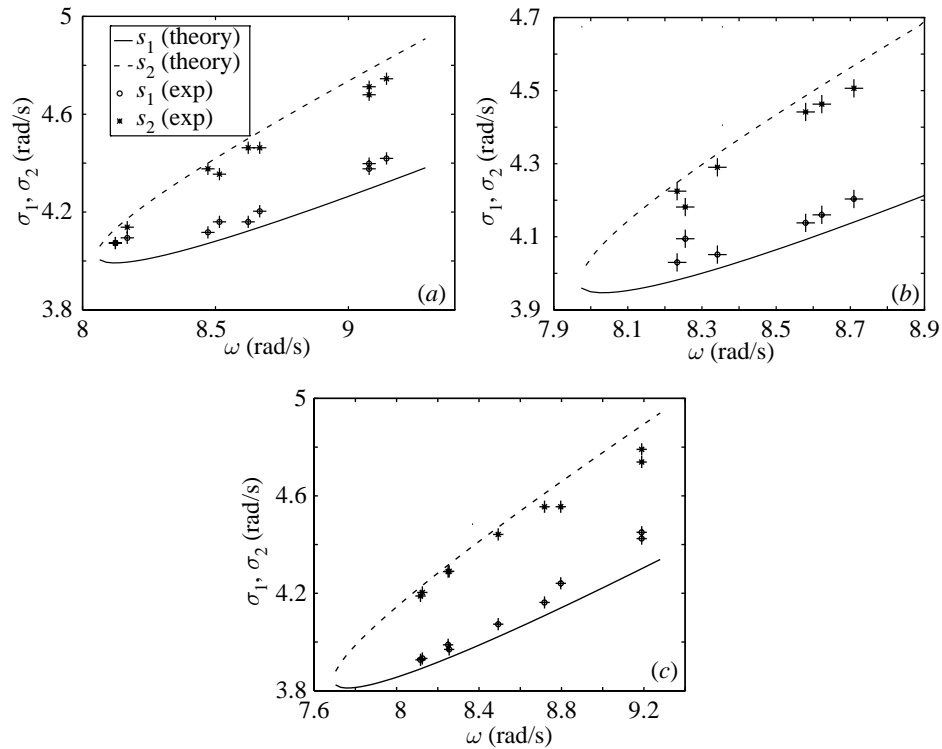
Figure 6. Theoretical and experimental internal-wave frequencies as functions of ω. Error bars indicate uncertainty in determining ω, σ_1 and σ_2: (a) $H = 10.5$ cm, $h = 10.6$ cm, $\gamma = 0.85$, $\lambda_z = 20.6$ m^{-1}; (b) $H = 12.5$ cm, $h = 7.9$ cm, $\gamma = 0.85$, $\lambda_z = 20.6$ m^{-1}; (c) $H = 13.6$ cm, $h = 5.5$ cm, $\gamma = 0.85$, $\lambda_z = 20.6$ m^{-1}.

Moving on to the nonlinear results, it must be stressed that the initial goal of the authors was to simply predict the frequency band within which growth would occur. However, the success of the experiments in confirming the linear results strongly motivated a comparision between the exponential growth rates predicted by the theory and those that could be estimated from the experiments.

As was discussed in the section on experimental procedure, the use of mineral oil as an upper layer precluded the use of resistance wave gauges to record the displacement of the free surface and hence the surface-wave amplitude. Instead, the FFT of the interfacial data and linear wave theory were used to calculate the amplitude of the surface wave. At the beginning of each experimental run, before significant evolution of the subharmonic internal waves, the interface would oscillate in phase with the surface wave, with a reduced amplitude. By performing a Fourier transform on this portion of the recorded data, an accurate measure of this reduced amplitude was obtained. The amplitude of the wave at the free surface was then inferred from the following equation from linear theory:

$$A = \frac{A_{\mathrm{r}}}{\cosh(kH) - (gk/\omega^2)\sinh(kH)}.$$

It must be acknowleged that the use of linear theory in the case of finite-amplitude waves is expected to introduce an error of the order of ϵ.

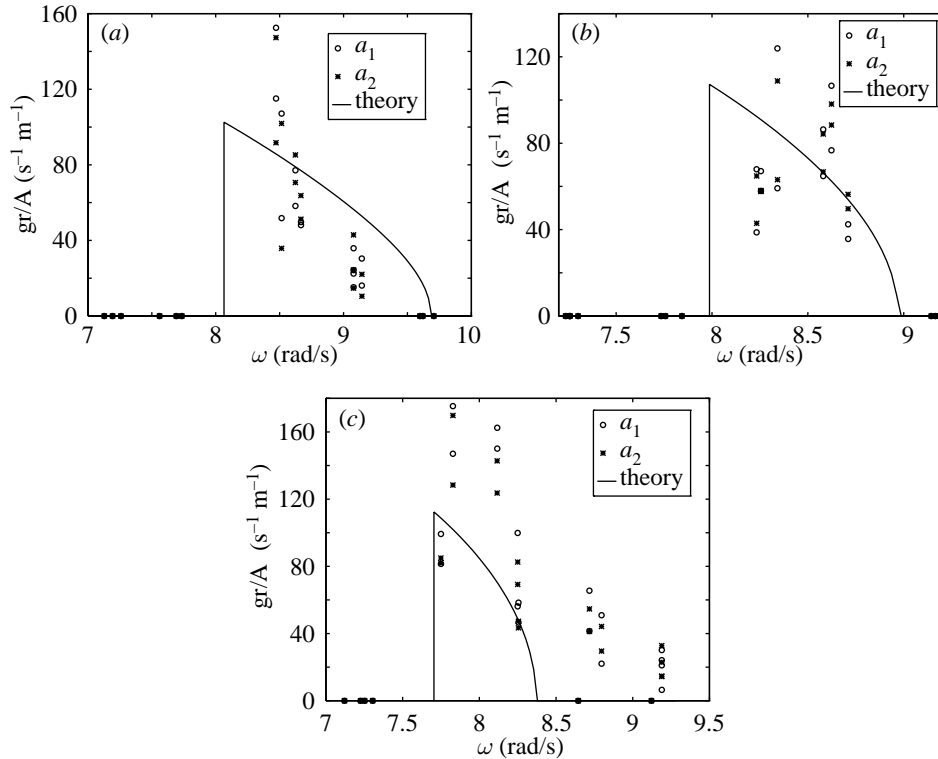To obtain the experimental values of interfacial growth rate, the results from the

Figure 7. Theoretical and experimental growth rates as functions of ω. Note that growth rates are normalized with respect to surface-wave amplitude: (*a*) $H = 10.5$ cm, $h = 10.5$ cm, $\gamma = 0.85$, $\lambda_z = 20.6$ m^{-1}; (*b*) $H = 12.5$ cm, $h = 7.9$ cm, $\gamma = 0.85$, $\lambda_z = 20.6$ m^{-1}; (*c*) $H = 13.6$ cm, $h = 5.5$ cm, $\gamma = 0.85$, $\lambda_z = 20.6$ m^{-1}.

harmonic analysis were plotted on a semilog axis and a linear regression was then performed to find the best straight-line fit. In many of the experimental runs, the internal-wave amplitudes were found to level off at steady-state values. As such, the results of their hamonic analyses could be divided into two regions; one of initial exponential growth, and one of equilibrium amplitude. The determination of the dividing point between these two regions involved an amount of subjectivity.

The comparisons between theory and experiment for the three depth configurations are detailed in figures 7*a*–*c*. The vertical axis is scaled as growth rate (gr) divided by the amplitude of the surface wave, thereby normalizing the results with respect to this parameter. Note that in each figure, there is a value of ω, the cutoff surface-wave frequency, below which no triad, and therefore no growth exists. As discussed, this is a consequence of the linear theory and is purely geometric. Furthermore, the maximum growth rate occurs right at this critical frequency. Additionally, there is an upper bound on ω, beyond which no growth exists. This limit is a result of the nonlinear analysis and corresponds to the threshold where the interaction coefficients change from having the same sign to having different signs. The result is that, with all other parameters fixed, instability occurs within only a very narrow band of surface-wave frequency.

The agreement between the theory and experiment is clearly not as good as it was for the linear theory. This is to be expected, in light of the issues mentioned above. However, figures 7*a*, *b* in particular demonstrate the clear success of the theory in
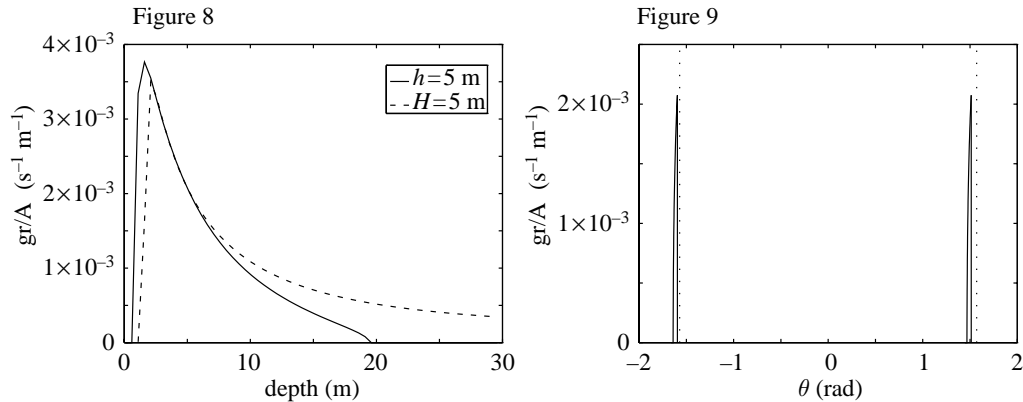
Figure 8. Variation of growth rate with fluid layer depth. The individual curves represent variation of one of the layer depths while the other is held fixed. $\gamma = 0.99$, $\omega = 0.6283 \text{ rad s}^{-1}$, $\lambda_z = 2.0 \text{ m}^{-1}$.

Figure 9. Variation of growth rate with angle of propagation relative to $\bar{k}$. Dotted lines denote angles of $\frac{1}{2}\pi$ and $-\frac{1}{2}-\pi$. $H = 5 \text{ m}$, $h = 5 \text{ m}$, $\omega = 0.6283 \text{ rad s}^{-1}$, $\gamma = 0.99$.

determining the band of surface-wave frequency within which instability occurs. The additional result that measured growth rates are found to be within a factor of two of those predicted by the theory is encouraging and motivates further, refined experimental efforts.

With these comparisons as validation, attention is turned lastly to the trends in growth rate with variation of the other physical parameters, as predicted by the theory. To place the results in the context of more realistic scales, conditions typical of an estuarine environment were considered.

Figure 8 details the effects of the fluid layer depths on the growth rates. Note that $\gamma = 0.99$ and $\omega = 0.6283 \text{ rad s}^{-1}$, corresponding to 10 s swell in a region of weak stratification. For each of the two curves, one of the layer depths is fixed and the other is variable. Linear analysis reveals that resonant triads exist for all values of H and h. However, figure 8 indicates that, at very low values of either H or h, there will be no growth observed. Due to the existence of triads even at these shallow depths, it can then be concluded that the absence of growth is a nonlinear, rather than a linear, effect. At the other extreme, as H becomes very large, the growth rate vanishes, while as h becomes very large, the growth rate asymptotes to a finite positive value. This is quite easy to explain from linear theory. Recall that quadratic interactions between any two of the waves are responsible for resonating the third. As the upper layer becomes infinitely deep, the value of Φ and its derivatives evaluated at $y = 0$ approach zero. Similarly, the values of the internal-wave potentials and their derivatives evaluated at $y = H$ approach zero. Therefore, the boundary forcing vanishes, yielding no growth of the internal waves. On the other hand, as the lower layer becomes infinitely deep, the boundary forcing at the interface and surface remains finite and there continues to be exponential growth of the internal waves.

Figure 9 details the directional spectrum of internal waves that will be generated by a specific monochromatic wave train. The growth rate is plotted as a function of θ, the angle between the wave vector of the surface wave and the wave vector of one of the internal waves. Note that the dashed lines indicate values of $\frac{1}{2}\pi$ and $-\frac{1}{2}\pi$. It is clear that the directional spectrum generated is very narrow-banded. Furthermore, it is clear that the internal waves generated are all very close to normal to the surface

wave. The usefulness of figure 9 is as follows: given the physical parameters of a certain environment (e.g. fluid-layer depths and stratification) and the frequency of the incoming surface waves, the initial temporal evolution of the interfacial wave field is specified.

The effect of stratification is found to be equivalent to that of surface-wave frequency and is only mentioned here in passing. A lower bound, below which no resonant triads exist is predicted by linear theory. An upper bound, one which is a consequence of the second-order theory, is also found, with the net effect that the growth of internal waves is confined to a narrow band of density ratio.

6. Concluding remarks

In an effort to develop a mechanism for the generation of internal waves by surface waves, an inviscid second-order nonlinear resonant interaction formulation has been pursued. The triad considered consists of a single progressive surface wave of finite amplitude and two perturbation internal waves. Fundamentally different from the works of previous authors, this approach is significant for several reasons. First, by requiring only a single surface wave, the formulation is valid in any situation where the surface-wave field is narrow-banded in frequency and direction. Second, since a single surface wave is now the primary carrier of energy, the internal waves are resonated by exponential, rather than linear, growth, demonstrating a much stronger interaction than has been shown before. And finally, the mechanism allows for a direct transfer of energy to short internal-wave wavelengths.

Linear analysis is used to determine the conditions for resonance and reveals that there are critical cut-off values of ω, γ and λ_z, beyond which it is impossible for resonant triads to exist. When the analysis is carried to second order, in order to determine the internal-wave growth rates, it is found that nonlinear bounds on all of the parameters of the problem exist. These bounds correspond to thresholds where the interaction coefficients go from having different signs to having the same sign. Beyond these threshold values, although a resonant triad exists, no exponential growth is predicted. The net effect of these various bounds is that instability of the internal waves, i.e. internal-wave growth, is found to be a very selective process, occurring under very specific conditions.

An experimental investigation into this mechanism of subharmonic internal-wave generation was undertaken and the results presented. Spectral analysis of the internal-wave records revealed that the measured internal-wave frequencies agreed extremely well with those predicted by the linear theory. In addition the theory proved successful in determining the frequency band within which growth would occur. Harmonic analysis of the records then allowed experimental growth rates to be estimated, and the results agreed reasonably well with the nonlinear theory.

The formulation presented is a useful predictive tool, indicating under what conditions significant internal-wave action in a stratified system will occur. It is hoped that knowledge of the presence and characteristics of this increased internal-wave climate will be of use to researchers interested in mixing and transport phenomena in stratified media.

It was found that the growth rates of the internal waves remained finite even as the lower-layer depth became very large. This suggests that the formulation may be well suited to thermocline dynamics and may be able to augment what is already known about the generation and distribution of internal-wave energy in the open

ocean. Along this line, it is well established that the buoyancy frequency in the ocean is typically much less than the frequency of incident swell. A typical value of the former is $0.001\,\mathrm{s}^{-1}$ while a characteristic value for the latter is $0.1\,\mathrm{s}^{-1}$. As such, internal waves subharmonic to swell frequencies would still be well above the buoyancy frequency, rendering this mechanism inappropriate. However, the authors wish to point out that at low latitudes, specifically between $28.8\,°\mathrm{S}$ and $28.8\,°\mathrm{N}$, the semi-diurnal tidal frequency is greater than twice the inertial frequency, but far less than the buoyancy frequency of the open ocean. As such, internal waves subharmonic to the semi-diurnal tide would have allowable frequencies. In other words, a path of interaction between the semi-diurnal barotropic tide and near-inertial baroclinic modes certainly does exist! Reformulation of the analysis to account for continuous stratification and planetary rotation will allow for consideration of such interactions.

Finally, the exponential growth predicted by this second-order formulation clearly describes initial growth only. By carrying the analysis to the third order, a description of the steady-state amplitudes of the internal waves can be obtained and compared to the experimental measurements.

Appendix A.

For the case of general fluid depths, the expressions for the interaction coefficients are so lengthy that the only practical way of handling them is to leave them as internal calculations in a symbolic software package such as Maple. However, they become more tractable in the asymptotic limits of deep or shallow fluid layers. For example, if the fluid layers are taken to be shallow with respect to all of the wavelengths, then the interactions are given by

$$\alpha_i = \left\{ \frac{\sigma_i}{h|\bar{\lambda}_i|^2} F_i + \frac{\gamma}{\sigma_i}\left(\frac{\sigma_i^2}{\gamma h|\bar{\lambda}_i|^2} - \frac{g(1-\gamma)}{\gamma} \right) G_i \right\} \left\{ \frac{2g\sigma_i(1-\gamma)}{h|\bar{\lambda}_i|^2} \right.$$

$$\left. - \frac{\gamma}{\sigma_i}\left(\frac{\sigma_i^2}{\gamma h|\bar{\lambda}_i|^2} - \frac{g(1-\gamma)}{\gamma} \right)\left(\frac{2g(1-\gamma)}{\gamma} - \frac{2\sigma_i^2(1-\gamma)}{\gamma h|\bar{\lambda}_i|^2} \right) \right\}^{-1}, \quad i = 1, 2.$$

The forcing functions are given by the following expressions:

$$F_2 = \left(1 - \frac{g(1-\gamma)Hk^2}{\omega^2} \right)\left(\frac{g\sigma_1}{h} + \frac{2gk\lambda_{1x}\sigma_1\sigma_2}{h|\bar{\lambda}_1|^2\omega} - \frac{g^2k^2(1-\gamma)}{\omega} \right)$$

$$- \left(\frac{\sigma_1^2}{\gamma h|\bar{\lambda}_1|^2} - \frac{g(1-\gamma)}{\gamma} \right)\frac{2\gamma gk\lambda_{1x}\sigma_2}{\sigma_1\omega} - \frac{\gamma g\sigma_1}{h},$$

$$G_2 = -\left(1 - \frac{g(1-\gamma)Hk^2}{\omega^2} \right)\frac{gk\sigma_1\sigma_2\lambda_{1x}}{h\omega|\bar{\lambda}_1|^2}$$

$$+ \left(\frac{\sigma_1^2}{\gamma h|\bar{\lambda}_1|^2} - \frac{g(1-\gamma)}{\gamma} \right)\left(\frac{g|\bar{\lambda}_1|^2}{\sigma_1} - \frac{gk^2}{\omega} + \frac{2gk\lambda_{1x}\sigma_2}{\sigma_1\omega} \right)$$

$$+ \frac{\sigma_1^2 gk\lambda_{2x}}{h|\bar{\lambda}_1|^2\omega} - \left(1 - \frac{g(1-\gamma)Hk^2}{\omega^2} \right)\left(\frac{\sigma_1^2}{\gamma h|\bar{\lambda}_1|^2} - \frac{g(1-\gamma)}{\gamma} \right)\left(\frac{g|\bar{\lambda}_1|^2}{\sigma_1} + \frac{gk\lambda_{1x}}{\sigma_1} \right),$$

$$F_1 = \left(1 - \frac{g(1-\gamma)Hk^2}{\omega^2}\right)\left(\frac{-g\sigma_2}{h} + \frac{2gk\lambda_{2x}\sigma_1\sigma_2}{h|\bar{\lambda}_2|^2\omega} + \frac{g^2k^2(1-\gamma)}{\omega}\right)$$
$$- \left(\frac{\sigma_2^2}{\gamma h|\bar{\lambda}_2|^2} - \frac{g(1-\gamma)}{\gamma}\right)\frac{2\gamma gk\lambda_{2x}\sigma_1}{\sigma_2\omega} + \frac{\gamma g\sigma_1}{h},$$

$$G_1 = -\left(1 - \frac{g(1-\gamma)Hk^2}{\omega^2}\right)\frac{gk\sigma_1\sigma_2\lambda_{2x}}{h\omega|\bar{\lambda}_2|^2}$$
$$+ \left(\frac{\sigma_2^2}{\gamma h|\bar{\lambda}_2|^2} - \frac{g(1-\gamma)}{\gamma}\right)\left(\frac{-g|\bar{\lambda}_2|^2}{\sigma_2} + \frac{gk^2}{\omega} + \frac{2gk\lambda_{2x}\sigma_1}{\sigma_2\omega}\right)$$
$$+ \frac{\sigma_2^2gk\lambda_{1x}}{h|\bar{\lambda}_2|^2\omega} + \left(1 - \frac{g(1-\gamma)Hk^2}{\omega^2}\right)\left(\frac{\sigma_2^2}{\gamma h|\bar{\lambda}_2|^2} - \frac{g(1-\gamma)}{\gamma}\right)\left(\frac{g|\bar{\lambda}_2|^2}{\sigma_2} - \frac{gk\lambda_{2x}}{\sigma_2}\right).$$

Other simplified forms of the interaction coefficients may be obtained by considering the limits of deep fluid layers and weak stratification.

References

Ball, K. 1964 Energy transfer between external and internal gravity waves. *J. Fluid Mech.* **19**, 465–478.

Brekhovskikh, L. M., Goncharov, V. V., Kurtipov, V. M. & Nangol'nykh, K. A. 1972 Resonant excitation of internal waves by nonlinear interaction of surface waves. *Izv. Akad. Nauk SSSR, Fiz-Atmos. Okeana* **8**, 192–203. (Engl. Transl. *Atmos. Oceanic Phys.* **8**, 192–197.)

Hasselmann, K. 1966 Feynman diagrams and interaction rules for wave–wave scattering. *Rev. Geophys.* **4**, 1–32.

Hill, D. F. & Foda, M. A. 1996 Subharmonic resonance of short internal standing waves by progressive surface waves. *J. Fluid Mech* **321**, 217–234.

Joyce, T. M. 1974 Nonlinear interactions among standing surface and internal gravity waves. *J. Fluid Mech* **63**, 801–825.

Lamb, H. 1932 *Hydrodynamics.* New York: Dover.

Lewis, J. E., Lake, B. M. & Ko, D. R. S. 1974 On the interaction of internal waves and surface gravity waves. *J. Fluid Mech.* **63**, 773–800.

Pierson, W. J. & Moskowitz, L. 1964 A proposed spectral form for fully developed wind seas based on the similarity theory of S. A. Kitaigorodskii. *J. Geophys. Res.* **69**, 5181–5190.

Thorpe, S. A. 1966 On wave interactions in a stratified fluid. *J. Fluid Mech.* **24**, 737.

Ting, C. K. F. & Raichlen, F. 1986 Wave interaction with a rectangular trench. *J. Waterway Port Coastal Ocean Engng ASCE* **112**, 454–460.

Watson, K. M., West, B. & Cohen, B. I. 1976 Coupling of surface and internal gravity waves: a mode coupling model. *J. Fluid Mech.* **77**, 185–208.